Electronic Supplementary Material (ESI) for Environmental Science: Nano.

Supplementary Material for

Confined ultrasmall MOF nanoparticles anchored on 3D-graphene network as efficient and broad pH adaptive photo Fenton-like catalysts

Heng Shi[a,b], Yi He[a,b,c,*], Yubin Li[d], Teng He[a,b] , Pingya Luo[a,b,*]

a. College of Chemistry and Chemical Engineering. Southwest Petroleum University, Sichuan 610500, P. R. China.

b. Oil & Gas Field Applied Chemistry Key Laboratory of Sichuan Province, Southwest Petroleum University, Sichuan 610500, P. R. China.

c. State Key Laboratory of Oil & Gas Reservoir Geology and Exploitation, Southwest Petroleum University.

d. School of New Energy and Materials, Southwest Petroleum University, Sichuan 610500, P. R. China.

*Corresponding author, Email: chemheyi@swpu.edu.cn

*Corresponding author, Email: luopy@swpu.edu.cn

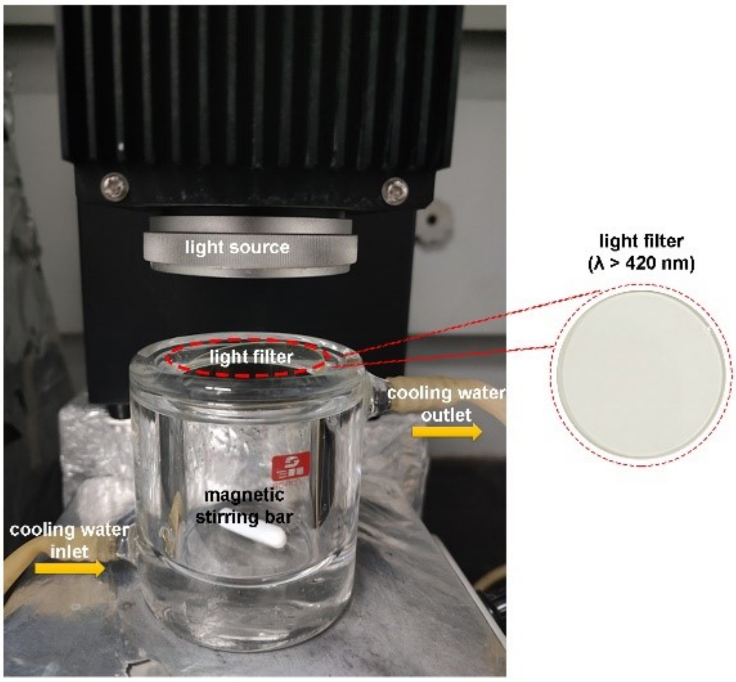

Figure S1. Photographs of the photocatalysis equipment and the visible light filter.

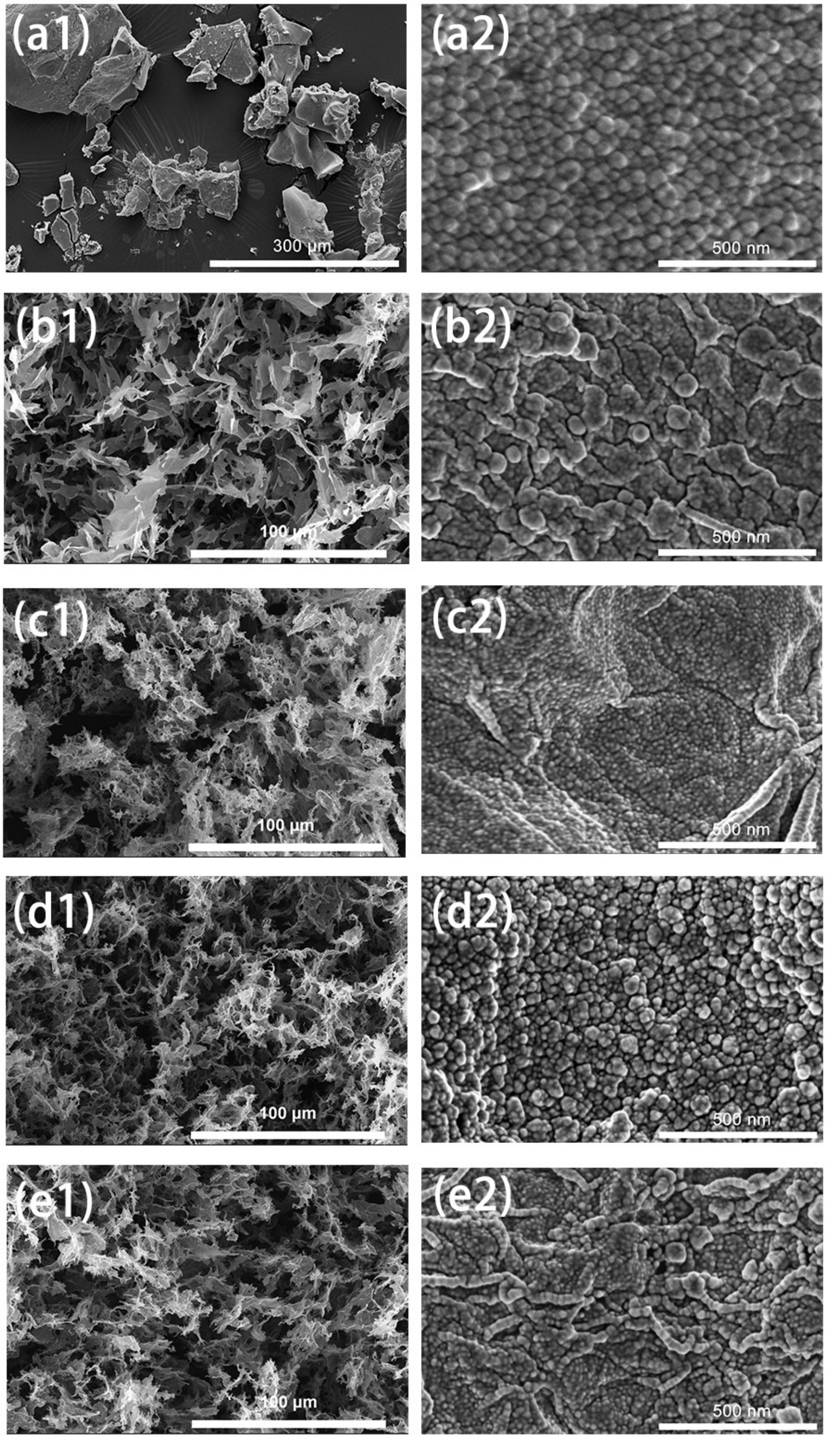

Figure S2. SEM image of (a1 and a2) PBA, (b1 and b2) PG, (c1, c2) PPG, (d1 and d2) PG-350, and (e1, e2) PPG-350 at different magnification.

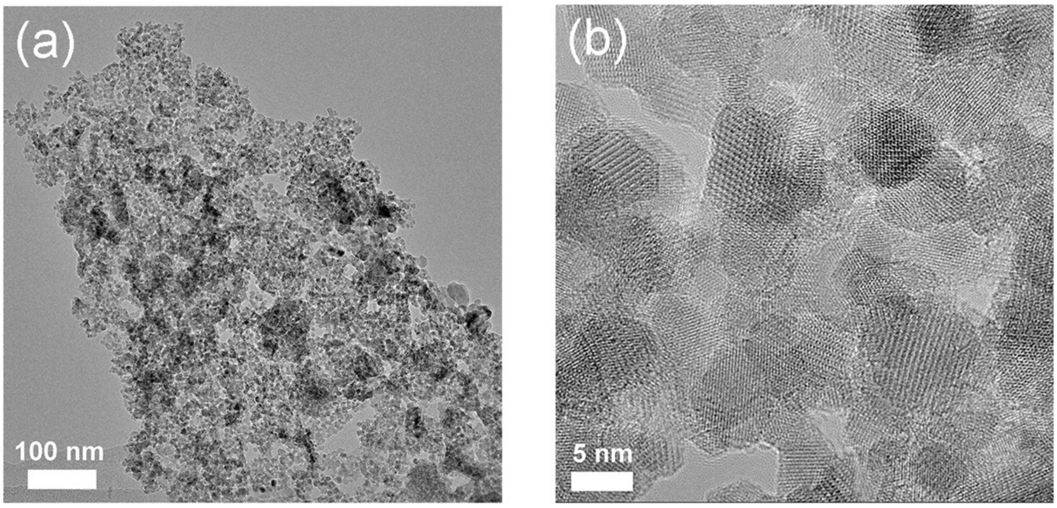

Figure S3. (a and b) TEM image of PG-350 at different magnification.

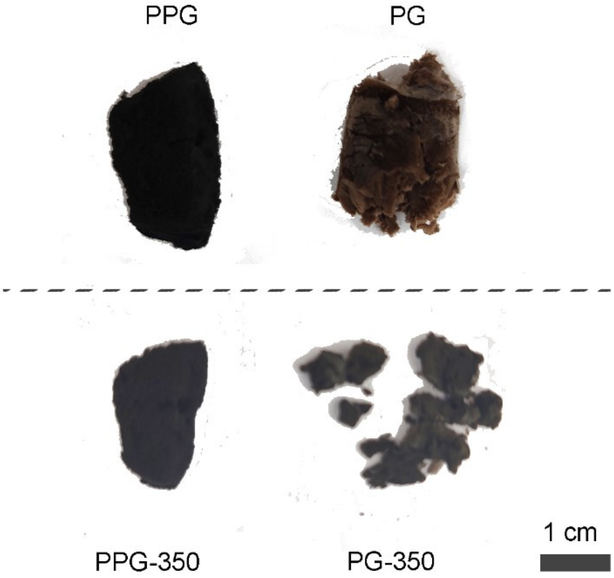

Figure S4. Macroscopic photographs of the composites.

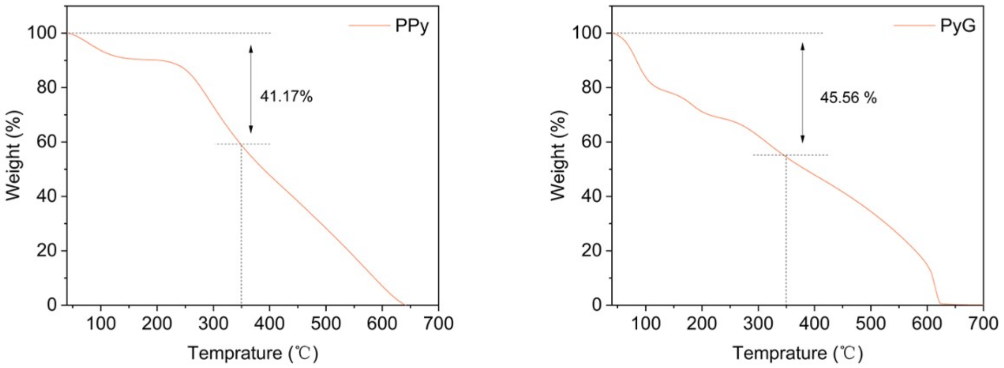

Figure S5. TGA curves of PPy and PyG in air with a heating rate of 10°C/min.

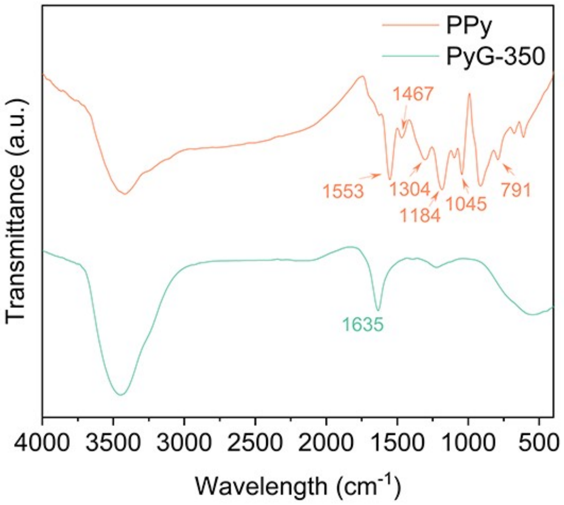

Figure S6. FTIR spectrum of PPy and PyG-350. For the spectrum of PPy, several typical peaks have emerged, including the peak at 791 cm-1 stands for the C-H out-of-plane deformation vibration of the polymer ring, the peak at 1184 cm-1 represents the stretching vibration of C-N bond, two peaks at 1304 cm-1 and 1045 cm-1 stands for C-H in-plane deformation vibration, and other two peaks at 1553 cm-1 and 1467 cm-1 represents antisymmetric and symmetric ring stretching modes. [1~3] While, the peak at 1635 cm−1 in the spectrum of PyG-350 is assigned to the C=C stretching vibration of the graphitic domains[1], and the characteristic peaks for PPy almost completely diminished, demonstrating its carbonization [4, 5].

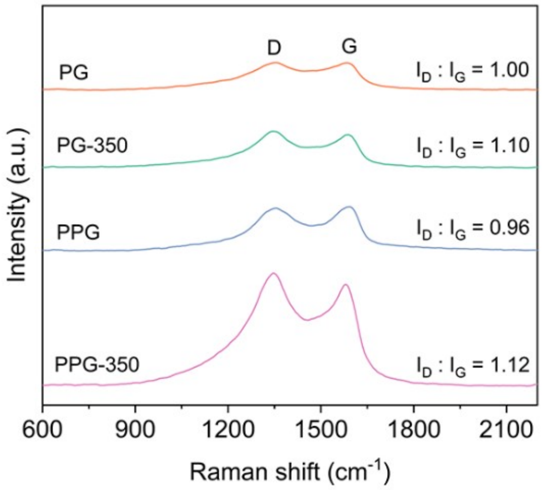

Figure S7. Raman spectra of PG, PPG, PG-350, and PPG-350.

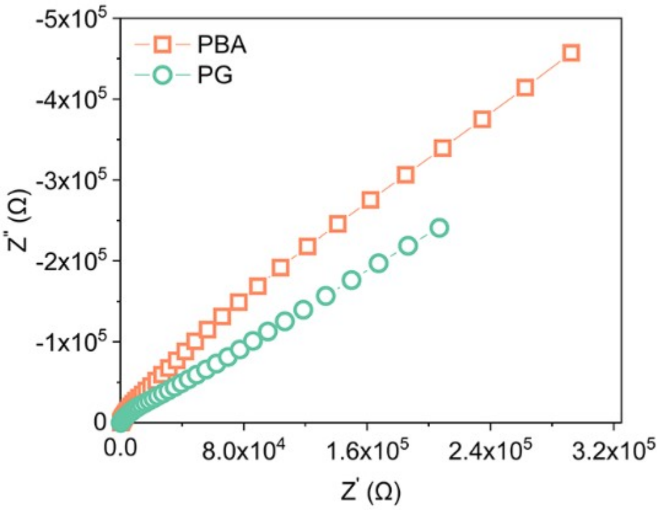

Figure S8. EIS plot of PBA and PG.

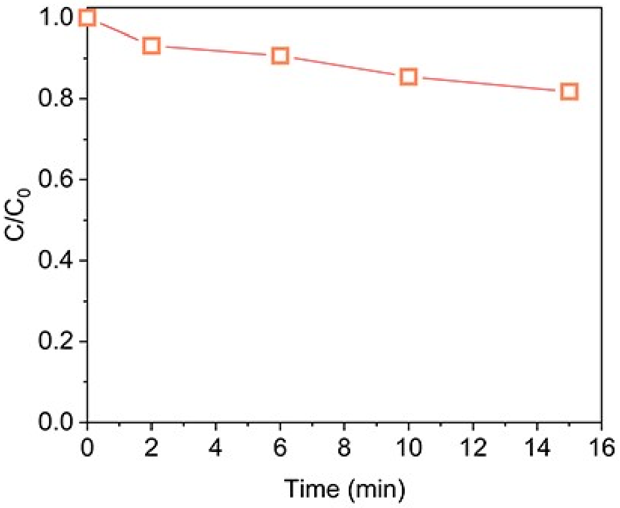

Figure S9. Degradation of TC in vis/PMS/PyG-350 system. (TC = 20 ppm, Catalyst = 50 mg·L^{-1}, PMS = 200 mg·L^{-1}, pH= neutral)

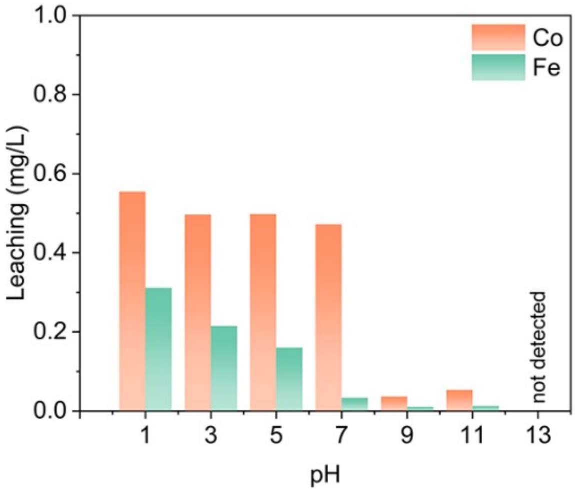

Figure S10. Metal ion leaching of PPG-350 under different pH conditions.

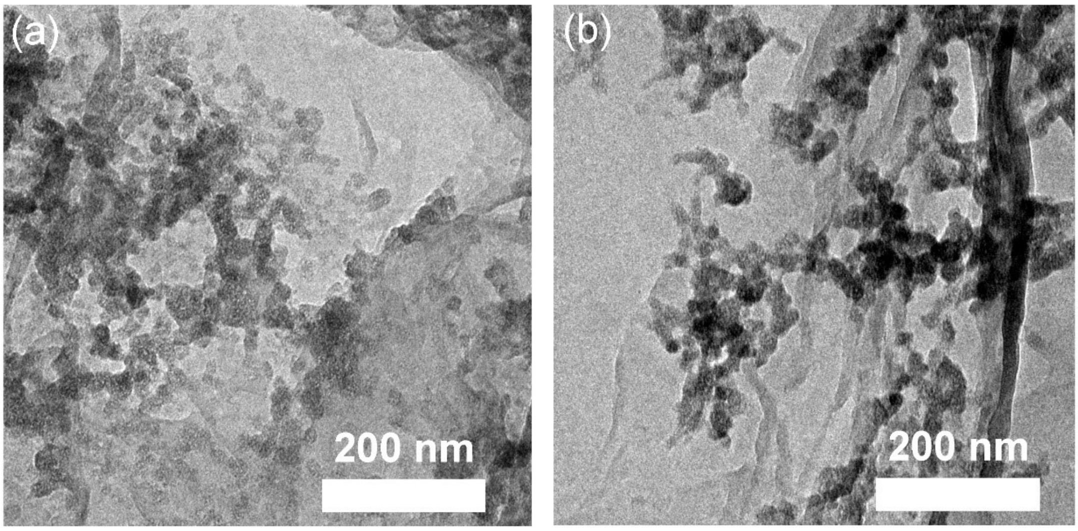

Figure S11. TEM images of the catalyst after working under (a) pH = 1 and (b) pH = 13.

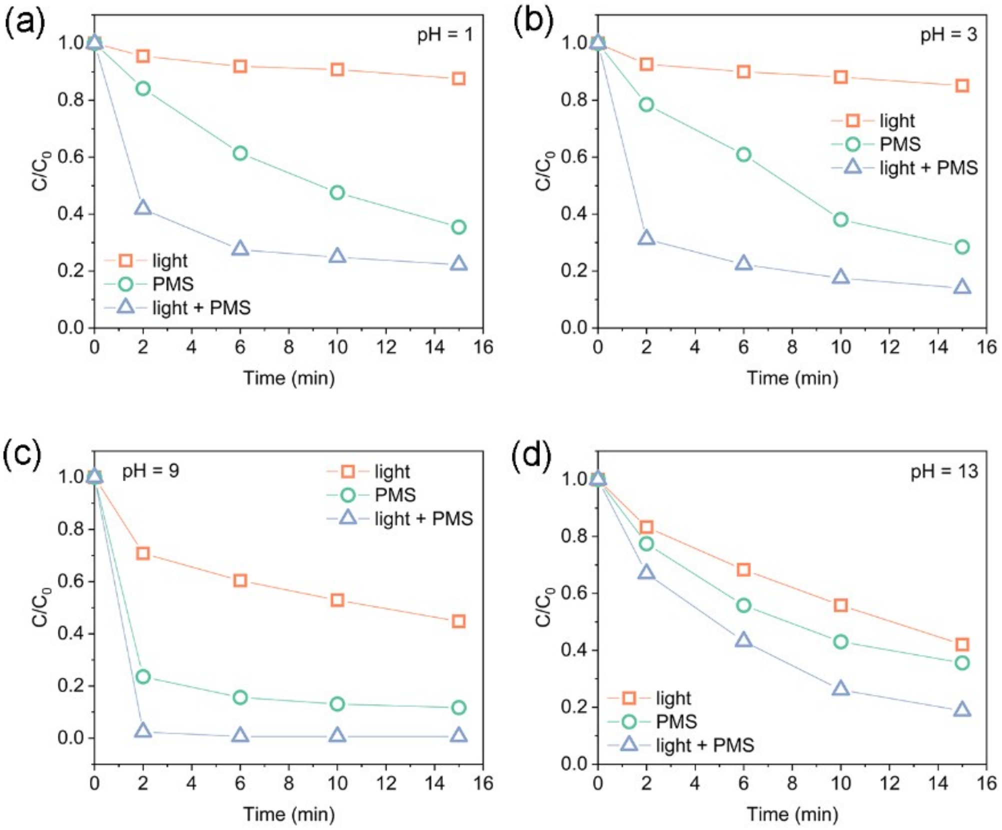

Figure S12. Degradation performance of PPG-350 under different pH (including 1, 3, 9, and 13) and various conditions (light, PMS, and light-PMS) (TC = 20 ppm, Catalyst = 50 mg·L^{-1}, PMS = 200 mg·L^{-1}).

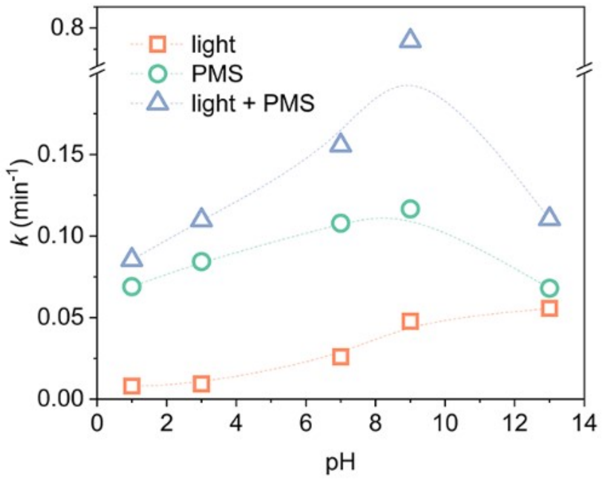

Figure S13. The degradation rate constant of TC by PPG-350 under different pH (including 1, 3, 9, and 13) and various conditions (light, PMS, and light-PMS).

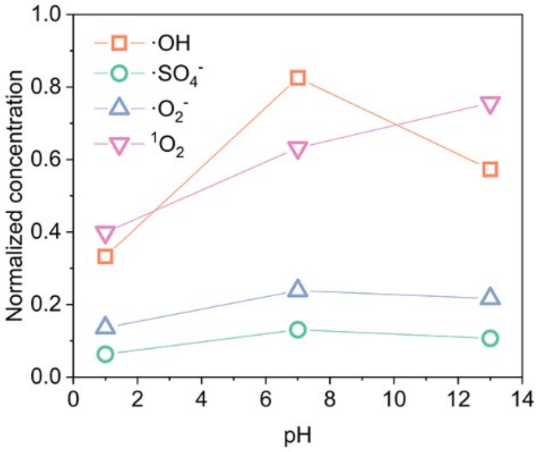

Figure S14. Relative concentration variation of different active species under different pH.

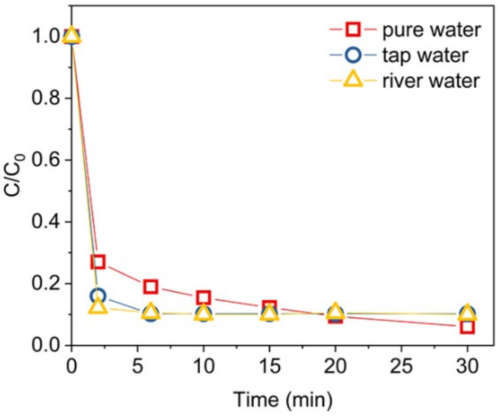

Figure S15. Degradation of TC in real water systems. (TC = 20 ppm, Catalyst = 50 mg·L^{-1}, PMS = 200 mg·L^{-1}).

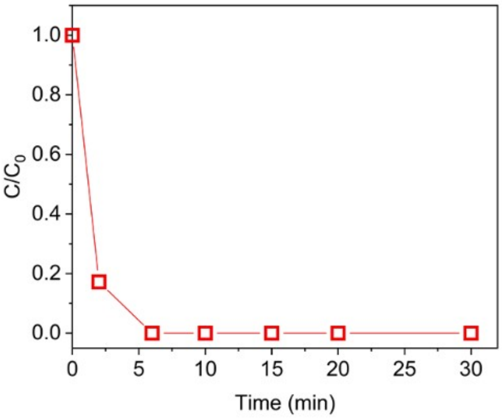

Figure S16. Degradation of low concentration of TC through Vis/PMS/PPG-350 system. (TC = 1 μg/L, Catalyst = 50 mg·L^{-1}, PMS = 200 mg·L^{-1}).

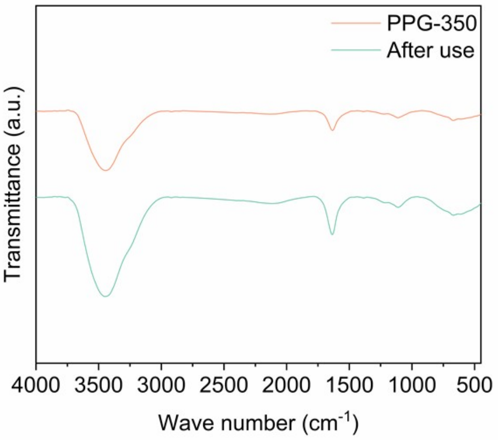

Figure S17. FTIR spectrum of PPG-350 before and after use.

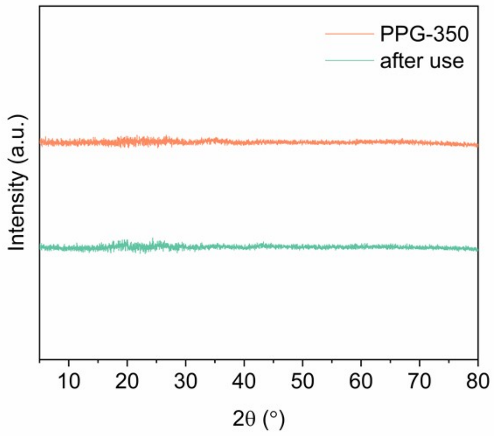

Figure S18. XRD spectrum of PPG-350 before and after use.

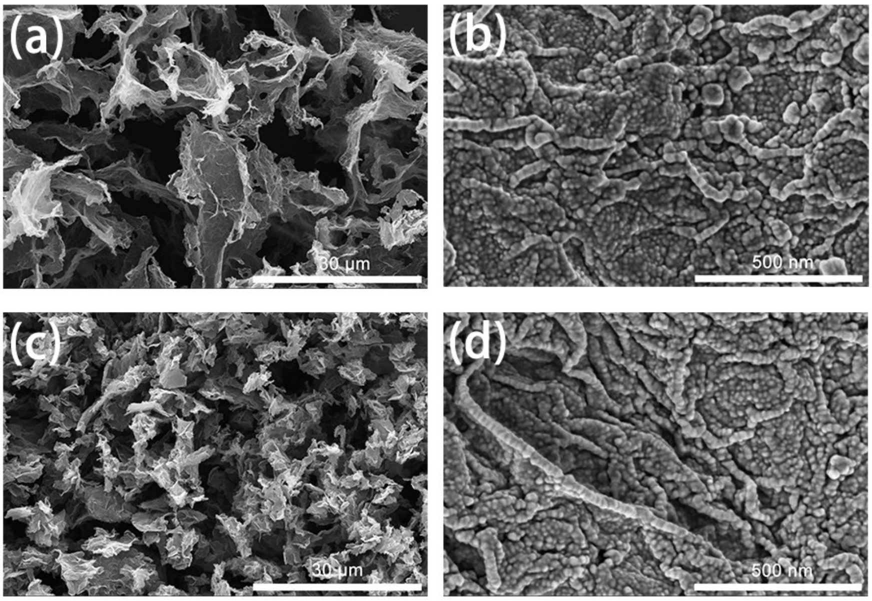

Figure S19. SEM image of PPG-350 before (a and b) and after use (c and d).

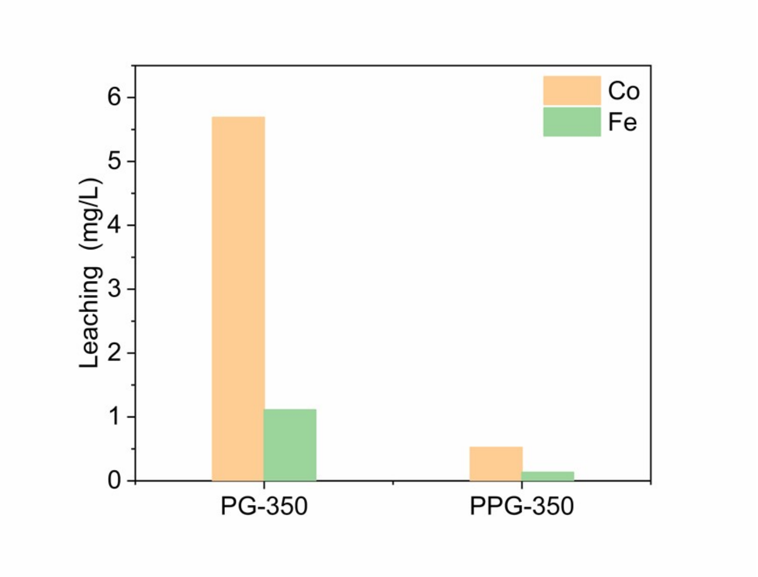

Figure S20. Metal leaching of PG-350 and PPG-350 after the catalytic experiment.

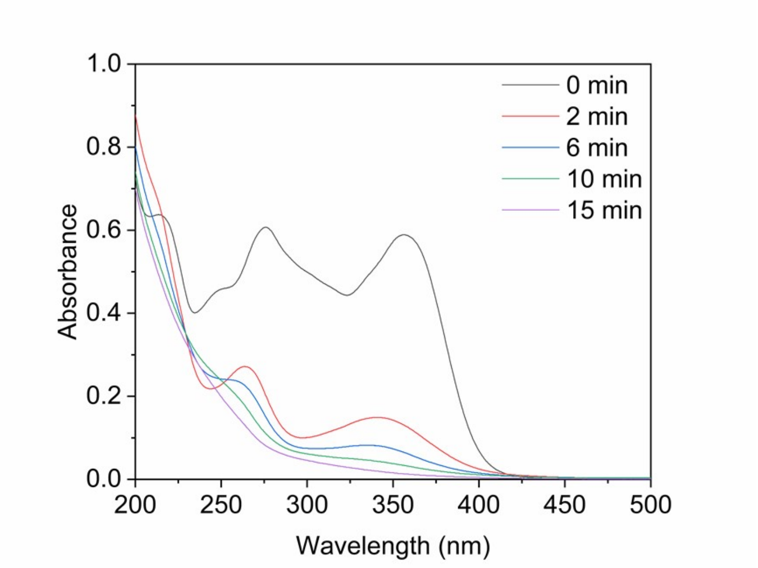

Figure S21. UV-vis spectra evolution of TC during the degradation test. (TC = 20 ppm, Catalyst = 50 mg·L^{-1}, PMS = 200 mg·L^{-1}, pH= neutral)

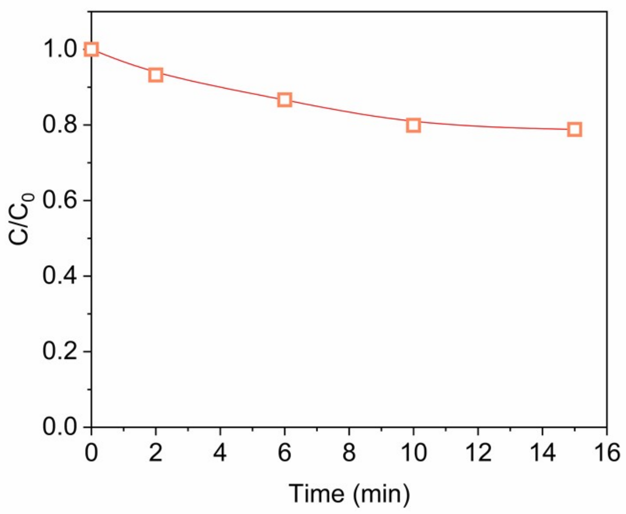

Figure S22. TOC change during the TC degradation via vis/PMS/PPG-350 system. (TC = 20 ppm, Catalyst = 50 mg·L^{-1}, PMS = 200 mg·L^{-1}, pH= neutral)

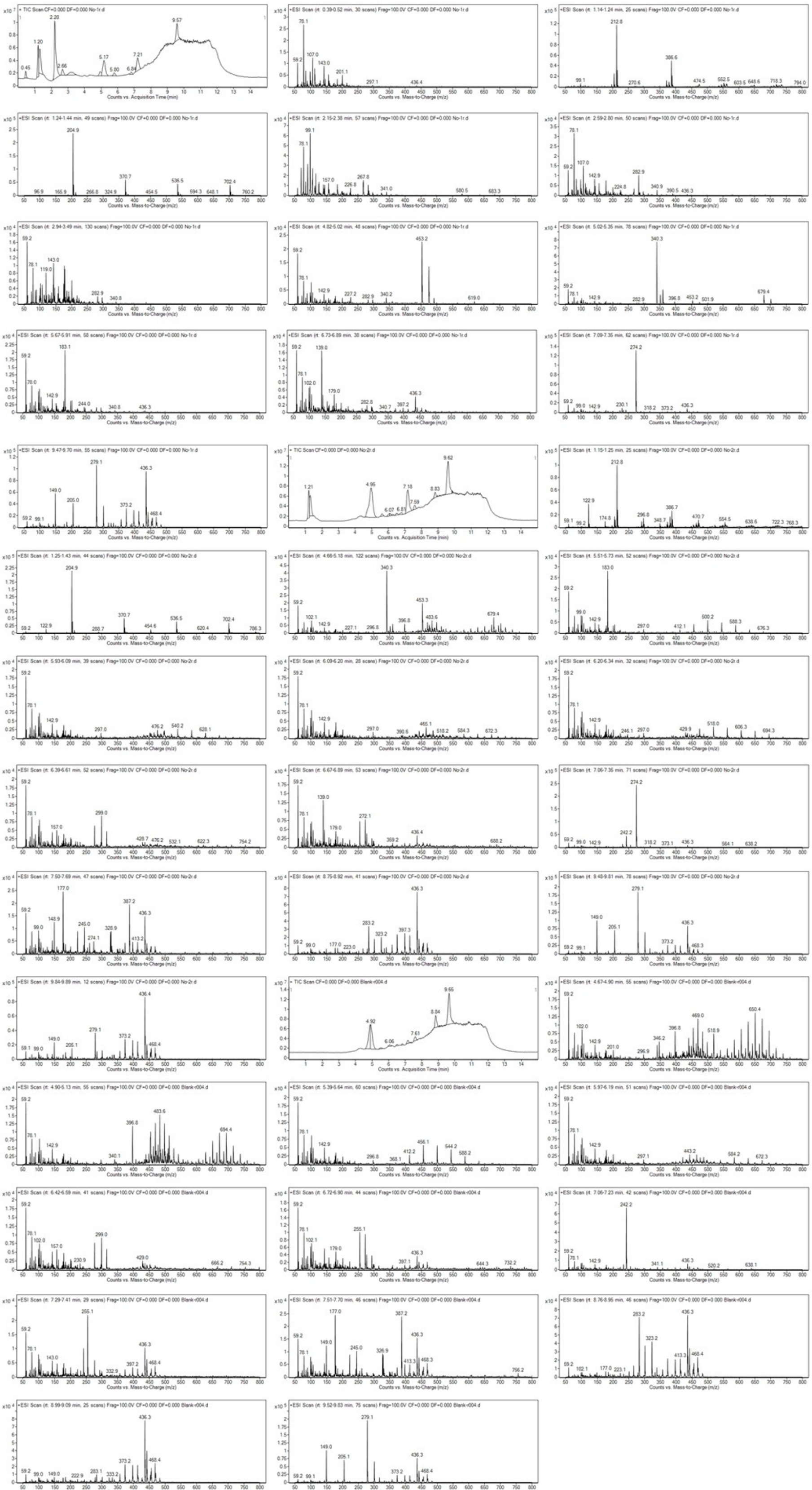

Figure S23. LC-MS results of the solution taken at 2 min and 15 min during the reaction, and the blank sample, respectively.

Table S1. Proposed structure of the degradation intermediates.

m/z	Formula	Proposed Structure
453	$C_{20}H_{24}N_2O_{10}$	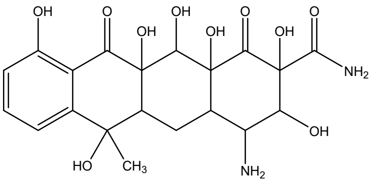
397	$C_{16}H_{16}N_2O_{10}$	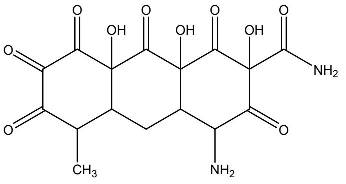
340	$C_{19}H_{17}NO_5$	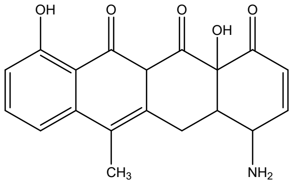
283	$C_{13}H_{14}O_7$	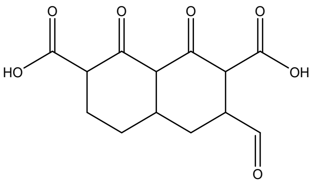
274	$C_{16}H_{18}O_4$	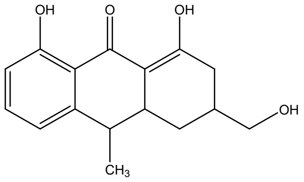
272	$C_{15}H_{12}O_5$	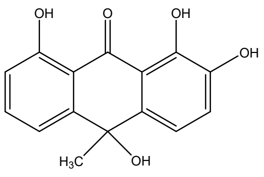
212	$C_{10}H_{12}O_5$	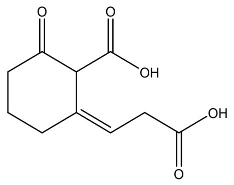
205	$C_{11}H_8O_4$	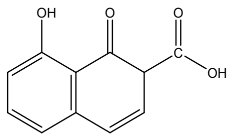

183	$C_9H_{10}O_4$	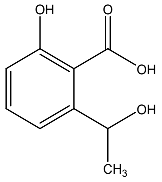
143	$C_7H_{10}O_3$	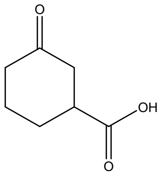
99	$C_6H_{10}O$	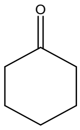

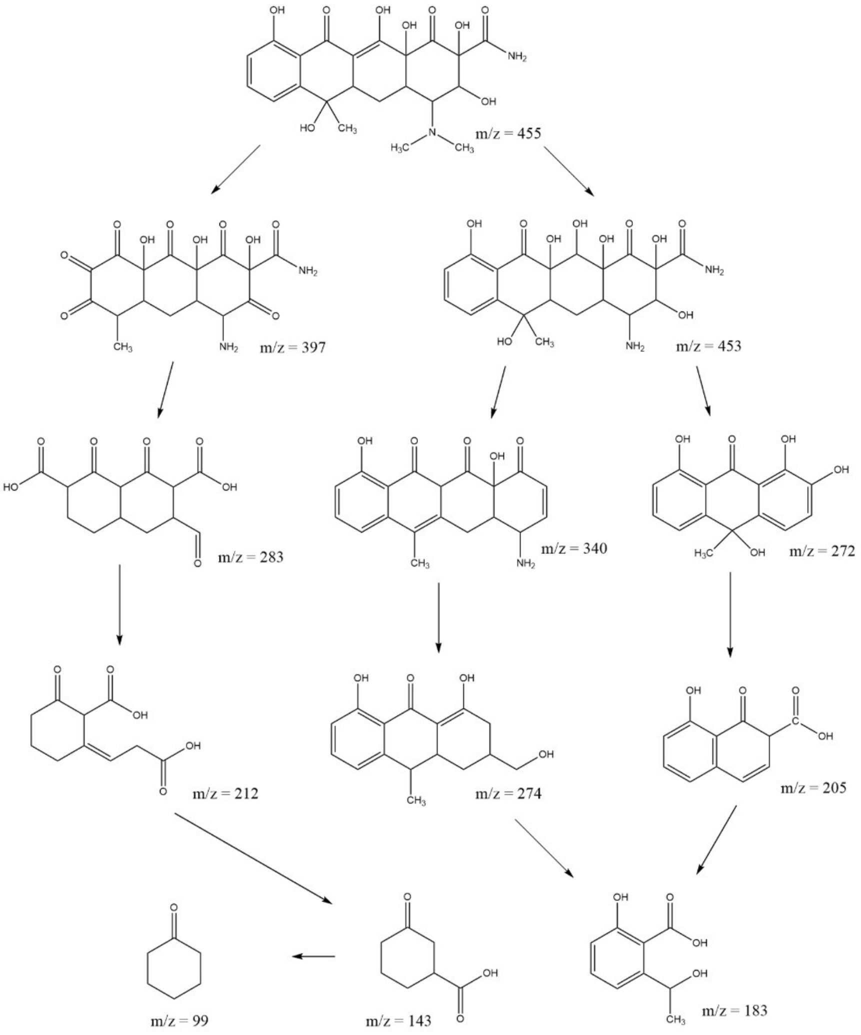

Figure S24. Possible degradation pathway of TC in vis/PMS/PPG-350 system.

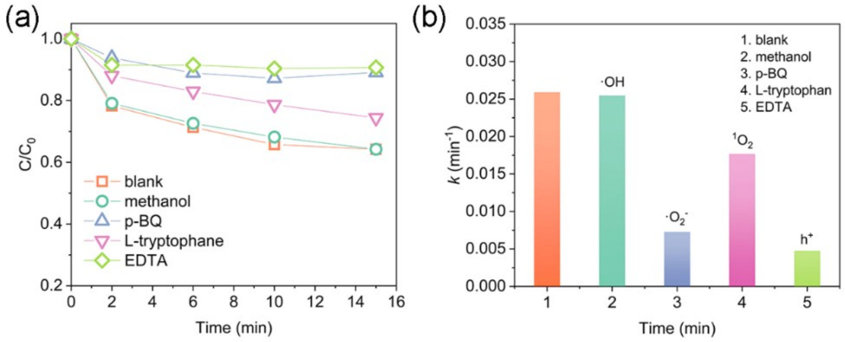

Figure S25. (a) Radical quenching test on Vis/PPG-350 system and corresponding (b) rate constant of various catalysts (TC = 20 ppm, Catalyst = 50 mg·L^{-1}, pH= neutral).

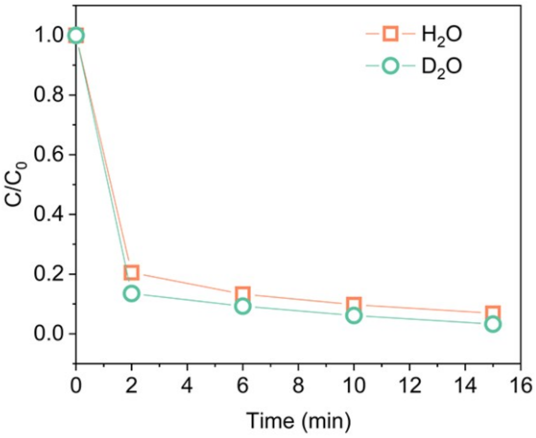

Figure S26. Degradation of TC in different solvent conditions. (TC = 20 ppm, Catalyst = 50 mg·L^{-1}, PMS = 200 mg·L^{-1}, pH= neutral)

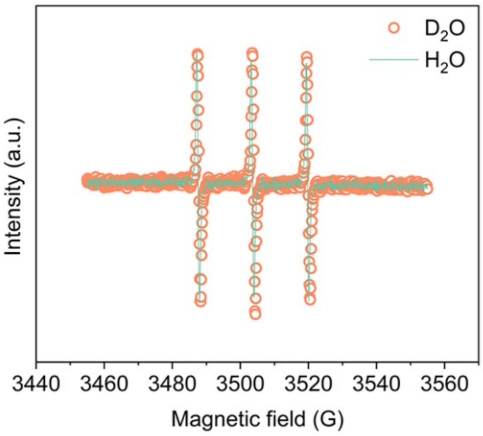

Figur S27. ESR signal of TEMP-$^1O_2$ obtained in D_2O and H_2O.

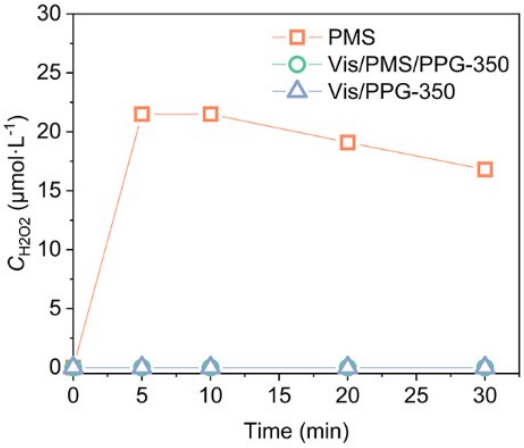

Figure S28. H_2O_2 concentration in different systems. The H_2O_2 concentration in both Vis/PPG-350 and Vis/PMS/PPG-350 systems by using titanium oxalate potassium as the indicator [6-7]. Unfortunately, no sign of H_2O_2 was observed. While we then have monitored the generation of H_2O_2 through the reaction between PMS and H_2O (Equation 1). As shown below, with 2g/L of PMS in water, about 21.5 μmol·L^{-1} of H_2O_2 has generated in 5 min, then the concentration of H_2O_2 starts to decrease, which is due to its decomposition (Equation 2 ~ 4). Herein, we think that it is caused by the fast reaction kinetics between iron/cobalt ions and H_2O_2 (Equation 5 ~ 6), and makes it rather difficult to track the trace of H_2O_2 in this system.

$$HSO_5^- + H_2O \rightarrow H_2O_2 + HSO_4^- \quad (1)$$

$$H_2O_2 + OH^{\cdot} \rightarrow H_2O + HO_2^- \quad (2)$$

$$H_2O_2 \rightarrow 2{\cdot}OH \quad (3)$$

$$\cdot OH + H_2O_2 \rightarrow HO_2\cdot + H_2O \quad (4)$$

$$Fe^{2+}/Fe(II)/Co^{2+}/Co(II) + H_2O_2 \rightarrow Fe^{3+}/Fe(III)/Co^{3+}/Co(III) + \cdot OH + OH^- \quad (5)$$

$$Fe^{3+}/Fe(III)/Co^{3+}/Co(III) + H_2O_2 \rightarrow Fe^{2+}/Fe(II)/Co^{2+}/Co(II) + \cdot OOH + H^+ \quad (6)$$

References

[1] Park H, Kim J W, Hong S Y, et al. Microporous polypyrrole-coated graphene foam for high-performance multifunctional sensors and flexible supercapacitors[J]. Advanced Functional Materials, 2018, 28(33): 1707013.

[2] Liu Y, Zhou J, Tang J, et al. Three-dimensional, chemically bonded polypyrrole/bacterial cellulose/graphene composites for high-performance supercapacitors[J]. Chemistry of Materials, 2015, 27(20): 7034-7041.

[3] Ballav N, Choi H J, Mishra S B, et al. Polypyrrole-coated halloysite nanotube clay nanocomposite: synthesis, characterization and Cr (VI) adsorption behaviour[J]. Applied clay science, 2014, 102: 60-70.

[4] Ma Y, Jiang S, Jian G, et al. CNx nanofibers converted from polypyrrole nanowires as platinum support for methanol oxidation[J]. Energy & Environmental Science, 2009, 2(2): 224-229.

[5] Liu B, Liu X, Yuan Z, et al. A flexible NO2 gas sensor based on polypyrrole/nitrogen-doped multiwall carbon nanotube operating at room temperature[J]. Sensors and Actuators B: Chemical, 2019, 295: 86-92.

[6] Zhang Z, Meng H, Wang Y, et al. Fabrication of graphene@ graphite-based gas diffusion electrode for improving H2O2 generation in Electro-Fenton process[J]. Electrochimica Acta, 2018, 260: 112-120.

[7] Zhao H, Shen X, Chen Y, et al. A COOH-terminated nitrogen-doped carbon aerogel as a bulk electrode for completely selective two-electron oxygen reduction to H2O2[J]. Chemical Communications, 2019, 55(44): 6173-6176.